Journal of Materials Science & Technology 278 (2027) 274–285

Contents lists available at ScienceDirect

Journal of Materials Science & Technology

journal homepage: www.elsevier.com/locate/jmst

Research Article

Ag-doped Cr_2AlC coatings with enhanced arc suppression and durability

Yingjie Wang[a,b], Yuxi Xu[b,c], Yiqun Feng[b], Kaiwei Yang[b,c], Qiang Wu[a,b], Guanshui Ma[b], Zhenyu Wang[b,*], Aiying Wang[b,c,*]

[a] School of Materials Science and Chemical Engineering, Ningbo University, Ningbo 315211, China
[b] State Key Laboratory of Advanced Marine Materials, Zhejiang Key Laboratory of Extreme-environmental Material Surfaces and Interfaces, Ningbo Institute of Materials Technology and Engineering, Chinese Academy of Sciences, Ningbo 315201, China
[c] Center of Materials Science and Optoelectronics Engineering, University of Chinese Academy of Sciences, Beijing 100049, China

ARTICLE INFO

Article history:
Received 10 February 2026
Revised 4 May 2026
Accepted 5 May 2026
Available online 22 May 2026

Keywords:
Arc erosion
MAX phase
Lath-like microstructure
Alloy/cladding layer

ABSTRACT

DC switching electrical contacts suffer from arc-driven thermal shock, material transfer, and rapidly rising contact resistance. Here, we develop Ag-doped Cr_2AlC MAX-phase coatings as arc-tolerant conductive layers and clarify the underlying degradation pathways. Cr_2AlC and Ag-Cr_2AlC coatings (~6.9 μm; Ag ~3.69 at.%) were deposited by hybrid cathodic arc-magnetron sputtering and annealed. Under 24 V DC/3 A make-break tests (1500 cycles), Cr_2AlC shows strong resistance fluctuations, a transient near-zero “welding” event, and rapid performance collapse after ~900 cycles, accompanied by increased arcing time and energy. In contrast, Ag-Cr_2AlC maintains stable arcing metrics with only mild late-stage fluctuations. TEM reveals a lath-like microstructure decorated by a continuous Ag-rich grain-boundary network that provides conductive percolation. Post-mortem mapping indicates that Ag activates under arc heating and reacts with transferred Cu to form a fluid Cu-Ag alloy/cladding layer, which displaces insulating products, builds low-resistance bridges, and suppresses crack propagation. This grain-boundary-enabled cladding mechanism breaks the resistance-Joule heating-arc persistence feedback and offers a general strategy for durable, low-resistance coated contacts.

© 2026 Published by Elsevier Ltd on behalf of The editorial office of Journal of Materials Science & Technology.

1. Introduction

Electrical contacts underpin switching and power distribution in transportation, aerospace, and marine systems, where reliability is governed by the stability of the contact interface under repeated make-break events [1,2]. In DC circuits, the absence of a current zero crossing sustains arc discharge, producing extreme local heating, material transfer, and rapid surface reactions that destabilize contact resistance and accelerate failure [3,4]. Silver-based contacts provide excellent conductivity but suffer from limited arc-erosion resistance and high cost, motivating architectures that couple a conductive support with a robust, arc-tolerant surface layer [5,6]. Developing contact surfaces that retain low resistance while resisting arc erosion and preserving structural stability, therefore, remains a central materials challenge.

MAX phases ($M_{n+1}AX_n$; M = early transition metal, A = group-13/14 element, X = C/N) combine metallic conductivity with ceramic-like stiffness and thermal stability, and their layered bonding can impart damage tolerance through kink and shear mechanisms [7–10]. Cr_2AlC, in particular, offers excellent oxidation resistance and thermal robustness, suggesting potential for anti-ablative contact surfaces. However, the conductivity of many MAX phases still falls short of stringent contact requirements, and repeated arc heating can trigger local decomposition, cracking, and erosion localization, undermining both electrical and mechanical function. Prior work has explored compositional tuning and grain-size control to improve conductivity and tailor arc response [11]. Incorporating highly conductive metal elements, such as Ag or Cu, is especially appealing: they can enhance current-carrying capacity and, owing to their relatively low melting points, promote a more distributed arc root, thereby reducing local energy concentration [12–16]. Most studies have pursued Ag/MAX bulk composites in which MAX phases reinforce an Ag matrix [9,17–20]; in contrast, many practical connectors and switching elements demand load-bearing substrates with dimensional stability, for which a coating-based

---

[*] Corresponding authors.
E-mail addresses: wangzy@nimte.ac.cn (Z. Wang), aywang@nimte.ac.cn (A. Wang).

https://doi.org/10.1016/j.jmst.2026.05.030
1005-0302/© 2026 Published by Elsevier Ltd on behalf of The editorial office of Journal of Materials Science & Technology.

strategy is more compatible but remains insufficiently understood [21,22].

Here, we develop Ag-doped Cr_2AlC MAX-phase coatings as functional surface layers for harsh DC switching. Trace Ag is used to engineer grain-boundary chemistry and electronic pathways, stabilizing a lath-like Cr_2AlC microstructure decorated by an Ag-rich intergranular network. By combining DC switching tests with post-mortem microstructural and compositional mapping, we link Ag redistribution and Cu transfer to the evolution of contact resistance and arc metrics. We show that Ag incorporation suppresses crack propagation and reshapes the erosion pathway from catastrophic brittle fracture to controlled, consumptive degradation, thereby improving arc-erosion stability and tolerance to subsequent corrosive attack. The results establish a coating-centric design principle for MAX-phase electrical contacts that reconciles conductivity with arc tolerance and structural integrity.

2. Experimental procedure

2.1. Coating preparation

Cr-Al-C-Ag coatings were deposited on Ni-based alloy substrates using a hybrid cathodic arc and magnetron sputtering system (Fig. 1(a)). A circular Cr target was employed as the cathodic arc source, while an AlAg alloy target was sputtered in magnetron mode. During deposition, a DC power of 0.8 kW was applied to the Cr target, and a DC sputtering power of 3.3 kW was set for the AlAg target. A reactive gas mixture of Ar/CH_4, with a flow rate ratio of 10:1, was introduced into the chamber. A -150 V pulsed DC negative bias was applied to the substrate. The total deposition time was 3 h. For undoped reference coatings, a Cr target (cathodic arc) and a pure Al target (magnetron sputtering) were used, while all other parameters were kept identical. After deposition, the samples were vacuum-annealed in a tube furnace (Fig. 1(b)): heated to 700 °C at 10 °C min^{-1}, held for 2 h, and furnace-cooled to room temperature, yielding the final Cr_2AlC and Ag-Cr_2AlC coatings.

2.2. Arc erosion test

Electrical contact (arc erosion) behavior was evaluated using a JF04C electrical contact testing system. For all experiments, 10 mm × 10 mm × 3 mm coated samples were fixed to function as the stationary cathode, opposing a pure Cu anode contact. The coatings were subjected to 1500 cycles in ambient air at 24 V DC and 3 A. Testing was conducted at 60 cycles min^{-1} with a 40 cN contact force and a 1 mm gap. Contact resistance, arcing time, and arc energy were tracked over the course of the procedure.

2.3. Characterization

Phase analysis of the coatings was performed using a high-power rotating anode multi-crystal X-ray diffractometer (XRD, Bruker D8 DISCOVER). The crystal structure of the coatings was further analyzed by transmission electron microscopy (TEM, Talos F200 X). Before and after the arc erosion experiment, the surface and cross-sectional morphology of the samples was examined using a thermal field-emission scanning electron microscope (SEM, Zeiss Sigma 300).

3. Results and discussion

3.1. Phase structure of coating

Fig. 2 presents the SEM surface morphology, elemental composition, and XRD phase structure of the as-prepared Cr_2AlC and Ag-Cr_2AlC coatings. The SEM micrographs indicate that both coatings, synthesized via the two-step process of hybrid cathodic arc-magnetron sputtering and subsequent annealing, exhibit macroparticles on their surfaces. The Ag-Cr_2AlC coating was successfully doped with 3.69 at.% Ag. After annealing, both coating systems show an observable interdiffusion layer with the substrate, and the final thickness of both coatings was approximately 6.9 µm. The XRD patterns, recorded in the 2θ range of 10°–90°, clearly display several high-intensity peaks for both coatings. These peaks correspond precisely to the Cr_2AlC MAX phase, as verified using PDF database card (No. 029-0017). Notably, due to the low concentration of Ag in the Ag-Cr_2AlC coating, no agglomerated elemental Ag phase was formed, and consequently, no distinct Ag peaks are visible in the XRD pattern.

3.2. Microscopic morphology of coatings

Fig. 3(a, b) shows BF and DF TEM images of the as-prepared Cr_2AlC coating. Unlike typical PVD-grown columnar grains, this coating features a dense equiaxed nanocrystalline structure [23], which inhibits ion diffusion and enhances thermal stability and oxidation resistance [24,25]. HRTEM analysis of a representative grain (Fig. 3(c, d)) confirms dense grain boundaries and the characteristic layered hexagonal structure of Cr_2AlC (space group $P6_3/mmc$). The measured c-lattice parameter of 1.28 nm and the corresponding SAED pattern (inset, Fig. 3(d)) align perfectly with standard Cr_2AlC

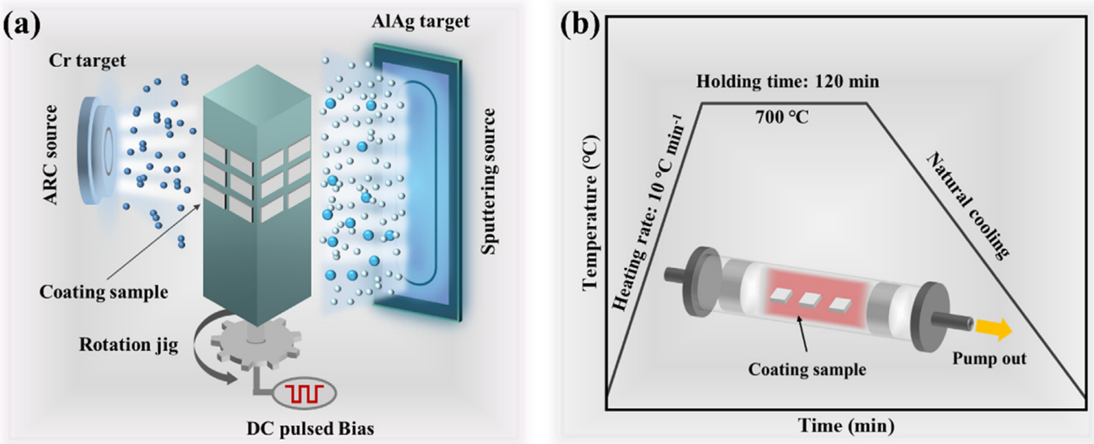

Fig. 1. Schematic diagram of (a) hybrid cathodic arc-magnetron sputtering equipment and (b) subsequent vacuum annealing procedure.

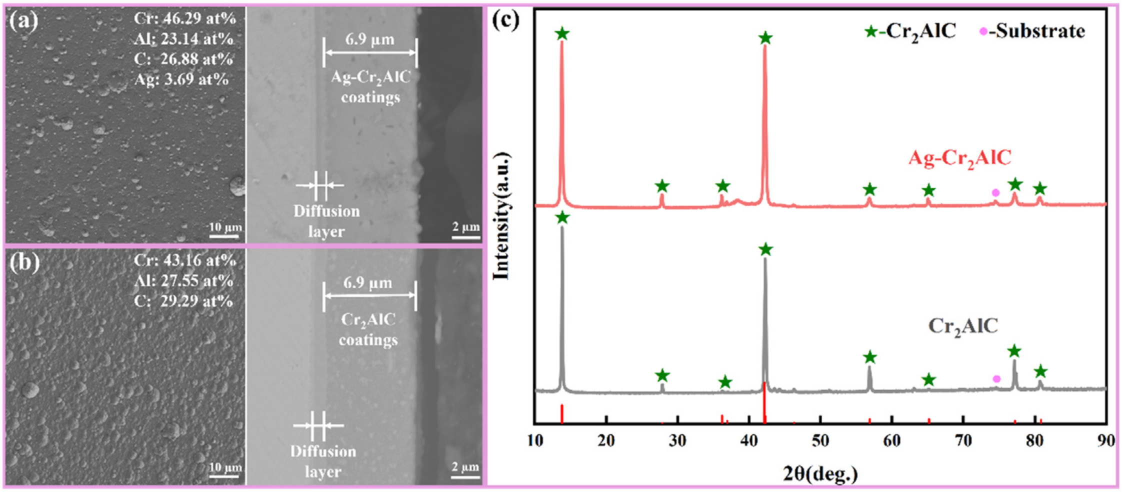

Fig. 2. Surface and cross-sectional morphologies of (a) Cr$_2$AlC coating and (b) Ag-Cr$_2$AlC coating. (c) XRD patterns of Cr$_2$AlC and Ag-Cr$_2$AlC coatings.

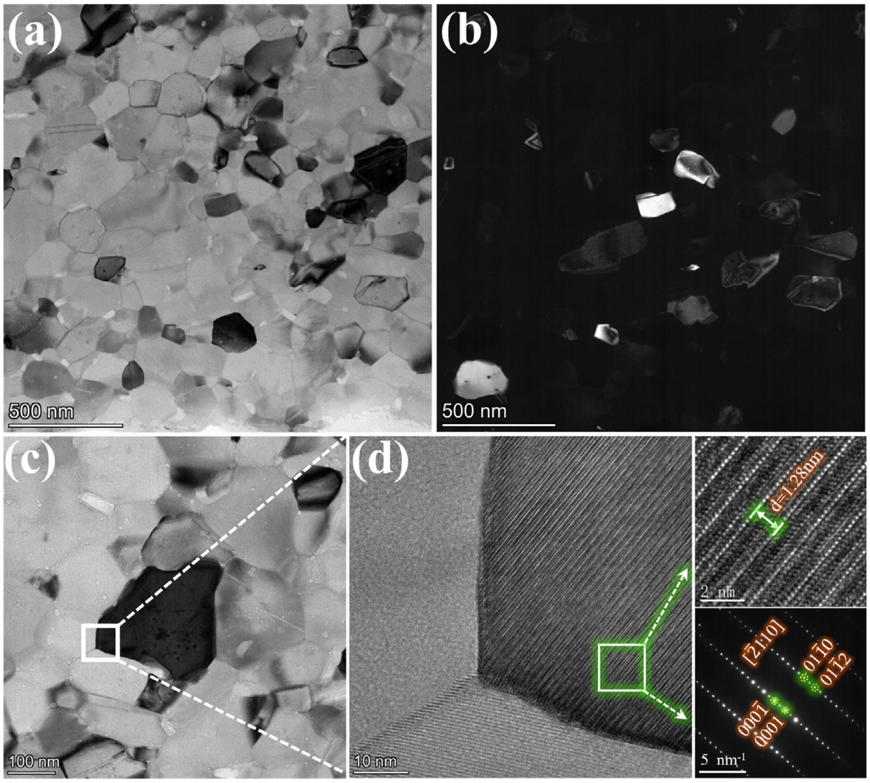

Fig. 3. TEM images of Cr$_2$AlC coating: (a) BF image; (b) DF image; (c) BF image of typical grains; (d) HRTEM image and SAED pattern.

MAX phase values, verifying its nanocrystalline nature and crystallographic orientation [25,26].

The BF/DF TEM images (Fig. 4(a, b)) reveal that Ag incorporation transforms the Cr$_2$AlC morphology into randomly oriented, fine lath-like grains. HAADF-STEM imaging (Fig. 4(c)) reveals a continuous, bright phase along the lath-like grain boundaries, indicating the segregation of high-atomic-number elements. Further analysis, combined with EDS mapping (Fig. 4(d)), reveals that the distribution of the Ag element highly overlaps with the bright regions in the HAADF image. Fig. 4(e) shows a typical lath-like grain, and Fig. 4(f) displays the HRTEM image of the grain interface. HRTEM imaging confirms a secondary phase at the grain boundary with an fcc atomic arrangement. Measurements show that the interplanar spacing of this phase is 0.24 nm, which aligns remarkably well with the characteristic interplanar spacing of elemental Ag [27]. This result strongly confirms that the Ag phase is uniformly distributed at the grain boundaries surrounding the Cr$_2$AlC grains, forming the characteristic microstructure of the Ag-Cr$_2$AlC composite. The crystal structure of Ag distributed along the Cr$_2$AlC grain boundaries is consistent with previous studies [28]. SAED (Fig. 4(g)) and lattice measurements (1.28 nm) confirm that the bulk remains high-purity Cr$_2$AlC, preserving its original MAX phase structure. The presence of this uniformly distributed soft Ag phase at the grain interfaces is anticipated to positively influence the composite material's electrical and thermal conduction properties.

3.3. Arc erosion performance of Cr$_2$AlC and Ag-Cr$_2$AlC coatings

Fig. 5(a) shows the make-break contact configuration in the JF04C electrical contact testing system. A fixed Cu tip serves as the

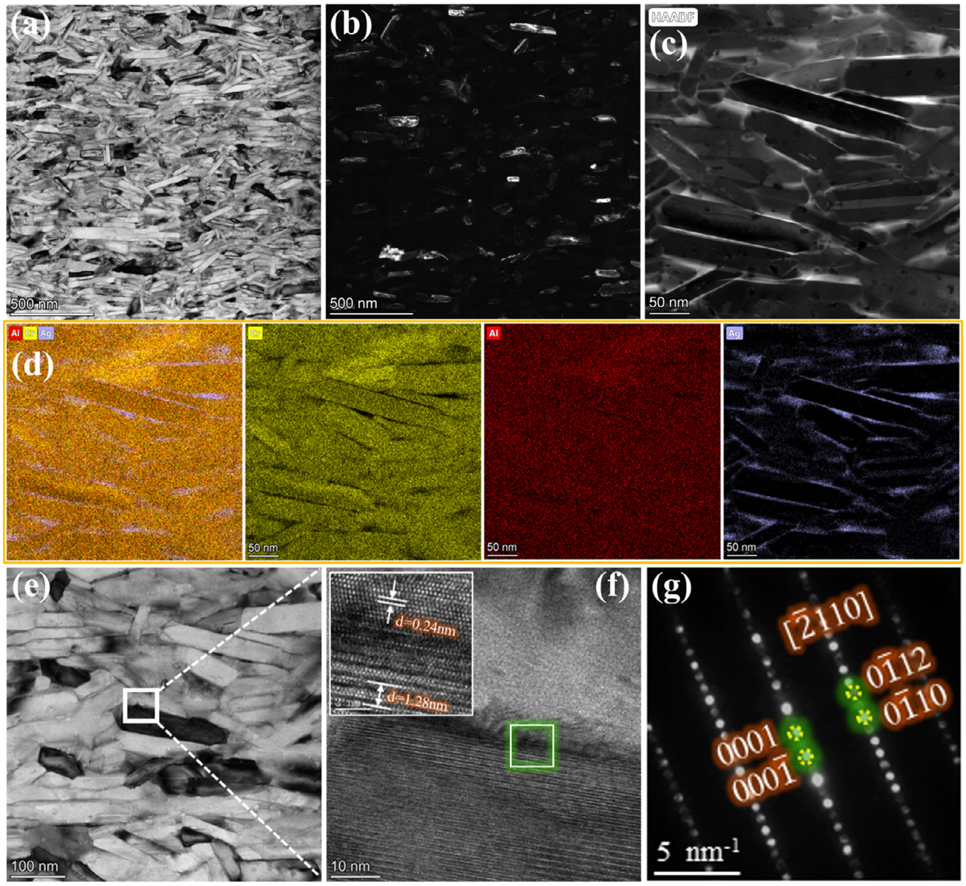

Fig. 4. TEM images of Ag-Cr_2AlC coating: (a) BF image; (b) DF image; (c) HAADF image; (d) corresponding elemental mapping of Cr, Al, and Ag; (e) BF image of typical grains; (f) HRTEM image; (g) HRTEM SAED pattern.

moving contact (anode), whereas the coated specimen, mounted to the stationary contact (cathode), acts as the counter-electrode. One cycle is defined as contact closure followed by separation. The JF04C system periodically records contact resistance, arcing time, and arc energy; their evolution with cycle number is summarized in Fig. 5(b–d).

As shown in Fig. 5(b), the Cr_2AlC coating exhibits pronounced resistance fluctuations during the early stage ($<$ 700 cycles), followed by a transient “valley” where the resistance approaches zero, and then a regime of markedly larger, unstable resistance. Low and stable contact resistance requires a persistent real contact area and high electrical conductivity [29]. The near-zero valley is consistent with a massive metallic contact event (local melting/welding) that briefly short-circuits the interface; the subsequent abrupt rise indicates severe and irreversible surface disruption after rupture of the welded junction. Although the addition of Ag refines Cr_2AlC into a lath-like microstructure, potentially compromising conductivity due to increased grain boundary scattering, the uniformly distributed Ag phase along the boundaries provides continuous, highly conductive pathways [30]. Consequently, the contact resistance of the Ag-Cr_2AlC coating remains stable for up to ~600 cycles, with only minor fluctuations thereafter (Fig. 5(b)), indicating improved contact stability and overall electrical performance.

The arcing time evolution (Fig. 5(c)) further differentiates the two coatings. Up to ~900 cycles, both samples sustain a low arcing time of ~0.07 ms, reflecting effective arc suppression and stable switching. Beyond ~900 cycles, the arcing time of the Cr_2AlC coating increases sharply, signalling accelerated degradation under arc erosion. Such increases typically arise from cumulative material loss, formation of resistive oxidation products, and progressive roughening that destabilize the contact interface and facilitate arc ignition and sustainment [31]. Consistently, the rise in contact resistance after ~900 cycles (Fig. 5(b)) amplifies Joule heating near separation, elevating the local temperature and further promoting arc persistence. By comparison, the Ag-Cr_2AlC coating retains a low, stable arcing time throughout the test, indicating a prolonged steady-wear regime with slow performance decay.

Arc energy trends (Fig. 5(d)) are quantified by [32]:

$$W_h = \int_0^t (U_0 - iR)i\mathrm{d}t + \frac{1}{2}LI^2 \tag{1}$$

where U_0 is the supply voltage, R is the circuit resistance, i is the instantaneous current, t is the arcing time, L is the circuit inductance, and I is the initial current before arcing. W_h represents the net energy delivered to the arc (source work minus resistive losses), with an additional contribution from inductive energy release during current interruption; the JF04C system accounts for the resistive term automatically. As expected, arc energy broadly scales with arcing time. Notably, even when arcing times are nearly identical at early cycles, the Cr_2AlC coating consistently shows higher arc energy than Ag-Cr_2AlC (Fig. 5(d)), implying a higher effective arc voltage. Sustained high arc energy imposes greater thermal and mechanical loads [33], accelerating erosion, oxidation, surface roughening, and eventual contact failure.

3.4. Arc erosion morphology of Cr_2AlC coating

3.4.1. Arc erosion surface morphology of Cr_2AlC coating

Fig. 6(a) shows the post-test surface morphology of the Cr_2AlC coating after 1500 make-break cycles. EDS mapping shows pro-

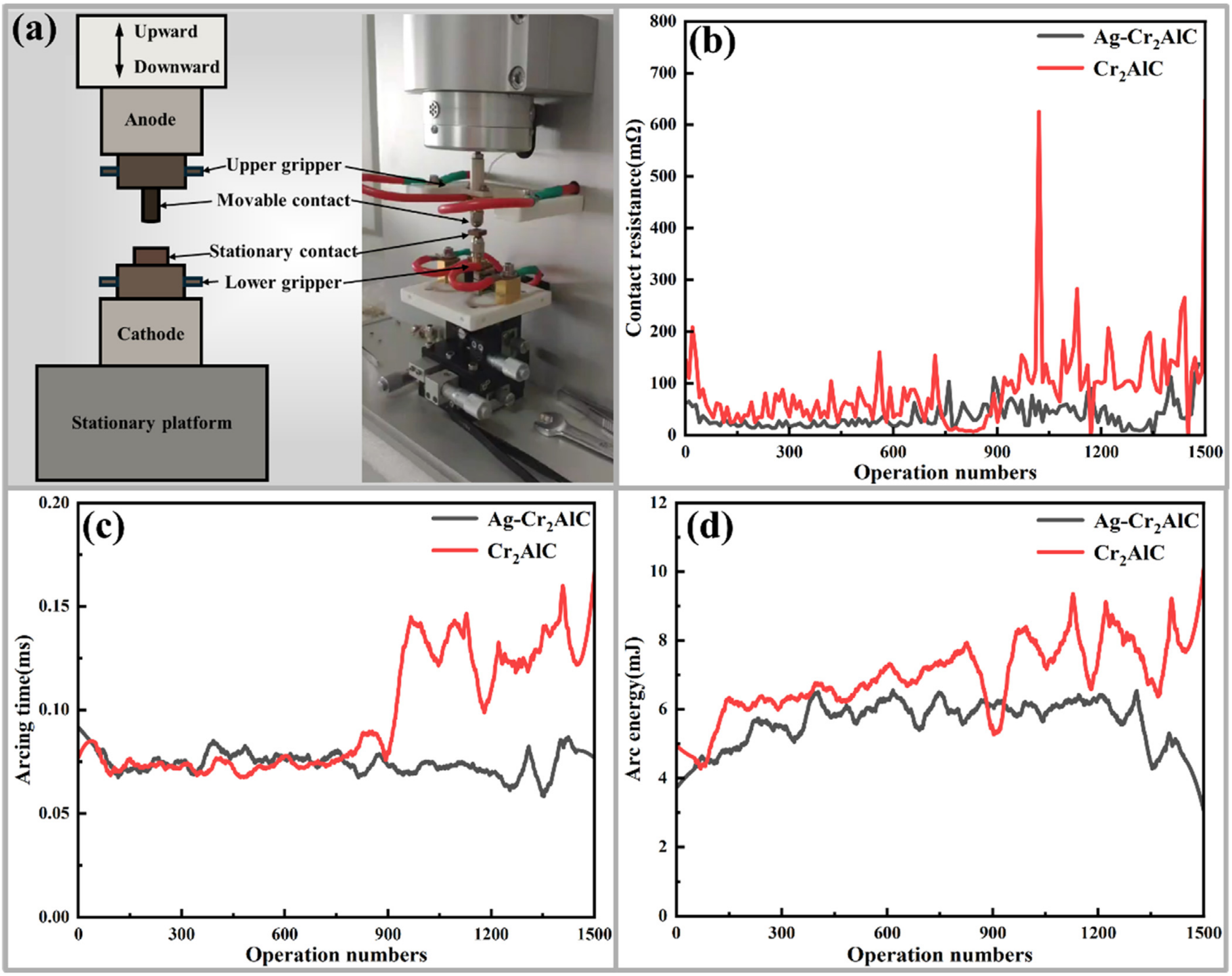

Fig. 5. (a) Schematic diagram of JF04C electrical contact equipment. (b) Contact resistance. (c) Arcing time. (d) Arc energy.

Table 1
Elemental compositions of the corresponding regions (Area (at.%)) in Fig. 6.

	Area 1	Area 2	Area 3	Area 4	Area 5	Area 6	Area 7
C	7.12	24.89	24.19	36.74	6.95	21.99	25.99
O	50.57	3.69	5.23	8.25	53.35	4.80	1.29
Al	18.78	0.54	1.36	0.75	23.81	22.28	24.40
Cr	17.86	4.07	61.59	45.14	12.15	38.13	15.07
Cu	5.68	66.81	11.84	9.12	3.70	12.80	33.24

nounced Cu enrichment from anode transfer. High local heat flux at the arc root causes Cu vaporization and droplet expulsion, resulting in its redeposition across the arc gap [34].

The erosion center (Fig. 6(b)) undergoes arc-induced Cr_2AlC dissociation. The corresponding element compositions are listed in Table 1. Due to high A-site reactivity [25,35], Al is preferentially extracted and oxidized to Al_2O_3. Strong Cr-C affinity promotes Cr_7C_3 formation (Area 3), with subsequent oxidation to Cr_2O_3 (Area 1) and carbon loss via volatilization. Simultaneously, transported Cu (Area 2) accumulates as granular and splashed deposits.

In the transition area (Fig. 6(c)), weaker thermal effects result in annular ridges and incomplete Cr_2AlC dissociation (Cr_7C_3, Area 4). Discontinuous Al/O mapping suggests reduced Al loss and mild oxidation compared to the center. The region is further characterized by mixed Cr-Al oxides (Area 5) and condensed Cu deposits, forming a cermet-like microstructure due to the lower temperature gradient.

Microcracks at the erosion boundary (Fig. 6(d)) result from high internal stresses exceeding the fracture strength, driven by thermal gradients and expansion mismatch [36]. While Cr_2AlC remains stable (Area 6), the boundary acts as a sink for Cu condensation and Al redistribution (Area 7). This reflects the differential mobility of the elements, where volatile Cu and Al migrate to cooler regions while Cr maintains its solid phase stability.

3.4.2. Arc erosion cross-sectional morphology of Cr_2AlC coating

Fig. 7(a) reveals the overall cross-sectional erosion morphology of the Cr_2AlC coating after 1500 make-break cycles. The micrograph unveils a high density of intracoating cracks and substantial interdiffusion with the substrate, corroborating the structural failure of the Cr_2AlC coating under sustained high-temperature arcing.

The central erosion area (Fig. 7(b)) exhibits a stratified architecture: an outermost Cu layer, an intermediate Cr-enriched layer (Area 1), and a Cr_2AlC coating. The corresponding element compositions are listed in Table 2. Al depletion in Area 1 indicates arc-induced Cr_2AlC decomposition into thermodynamically stable chromium carbides. The surface Al_2O_3 (Area 3) is absent due to polishing artifacts, where brittle fragments detached and trapped

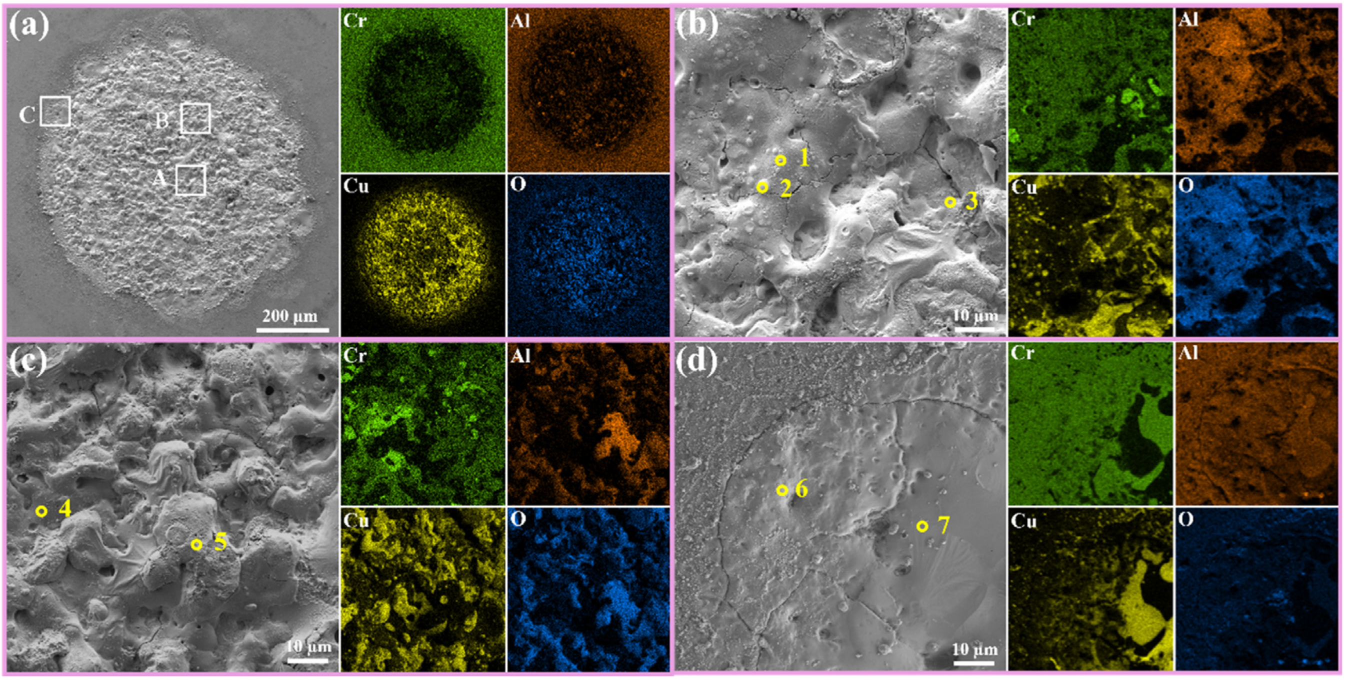

Fig. 6. (a) Arc erosion surface morphology of Cr_2AlC coating. (b) Central erosion area (Area A). (c) Transitional erosion area (Area B). (d) Edge erosion area (Area C).

Table 2
Elemental compositions of the corresponding regions (Area (at.%)) in Fig. 7.

	Area 1	Area 2	Area 3	Area 4	Area 5	Area 6
C	29.73	36.03	12.89	31.44	8.92	22.49
O	0.86	3.77	44.35	2.41	47.62	0.89
Al	5.68	13.82	22.22	3.18	30.16	6.46
Cr	48.70	11.73	16.33	60.33	10.61	57.92
Cu	15.03	34.65	4.21	2.65	2.68	12.25

Table 3
Elemental compositions of the corresponding regions (Area (at.%)) in Fig. 8.

	Area 1	Area 2	Area 3	Area 4	Area 5	Area 6
C	20.77	22.57	16.75	10.04	19.71	9.26
O	23.37	9.98	6.64	50.70	4.33	11.66
Al	3.52	0.79	13.67	27.85	16.22	36.45
Cr	12.39	54.95	13.73	3.14	52.43	12.05
Cu	38.24	11.61	37.49	8.19	3.07	7.07
Ag	1.71	0.10	11.72	0.08	4.24	23.51

in the resin. Furthermore, molten Cu penetrates deep cracks via capillary action. In the crack interior (Area 2), Al selectively dissolves into the Cu melt due to weak bonding and high solubility, accelerating structural degradation.

In the transition area (Fig. 7(c)), reduced thermal input results in a discontinuous Cu phase appearing as isolated islands. This suggests a viscous wetting mechanism rather than the violent splashing observed in the center. An Al_2O_3-based oxide layer, containing minor Cr (implying a Cr-Al composite oxide per Area 3 analysis), overlies the Cu melt. Beneath this lies a reaction layer dominated by the Cr_7C_3 phase (Area 4), while macroscopic cracks persist in the underlying Cr_2AlC.

The erosion boundary (Fig. 7(d)) consists of Al/Cr oxides, Cu particulates, and larger blocks. Selective oxidation is evident from the Al_2O_3 surface (Area 5) and subsurface chromium carbides (Area 6). Notably, interfacial cracks form between the oxide layer and Cu blocks, driven by (i) thermal mismatch stresses due to CTE disparities among the phases; and (ii) stress concentration from Cu solidification shrinkage.

3.5. Arc erosion morphology of Ag-Cr_2AlC coating

3.5.1. Arc erosion surface morphology of Ag-Cr_2AlC coating

Fig. 8(a) shows the surface erosion of the Ag-Cr_2AlC coating. The erosion pattern is non-circular, deviating from the regular geometry of pure Cr_2AlC. EDS mapping reveals a pronounced depletion of Cr and Al within the central zone, which spatially correlates with a concentrated Cu layer. Beyond the central area, Ag concentrates at the periphery of the Cu-rich zone. This distribution results from the outward diffusion and flow of intrinsic Ag induced by steep temperature gradients. The resulting liquid Ag-Cu phase permeates grain boundaries and matrix porosity, creating a distinctive erosion morphology.

Fig. 8(b) illustrates the central erosion area, which is dominated by the solidified Cu melt. The corresponding element compositions are listed in Table 3. In regions subjected to the most intense arc exposure, the coating exhibits clear signs of thermal decomposition. Elemental analysis of the Cr-rich region (Area 2) confirms severe Al depletion and the concomitant formation of thermodynamically stable chromium carbides. The spatial overlap and correlated increase of Ag and Cu signals (Area 1) indicate the formation of a Cu-Ag liquid alloy. This Ag incorporation enhances the melt's wettability on the ceramic surface, promoting the coalescence of larger, stable droplets.

The transition erosion area (Fig. 8(c)) features a smooth Cu-Ag metallic cladding. A compositional gradient characterized by diminishing Cu and increasing Ag toward the periphery suggests the formation of a low-melting-point Cu-Ag alloy liquid. Driven by superior fluidity and wettability, this phase spreads via surface tension to form a dense and conductive protective film. The Ag accumulation at the outer edge (Area 3) indicates that the flow velocity of intrinsic Ag exceeded that of deposited Cu. Additionally, the presence of Al_2O_3 precipitates (Area 4) suggests a mechanism

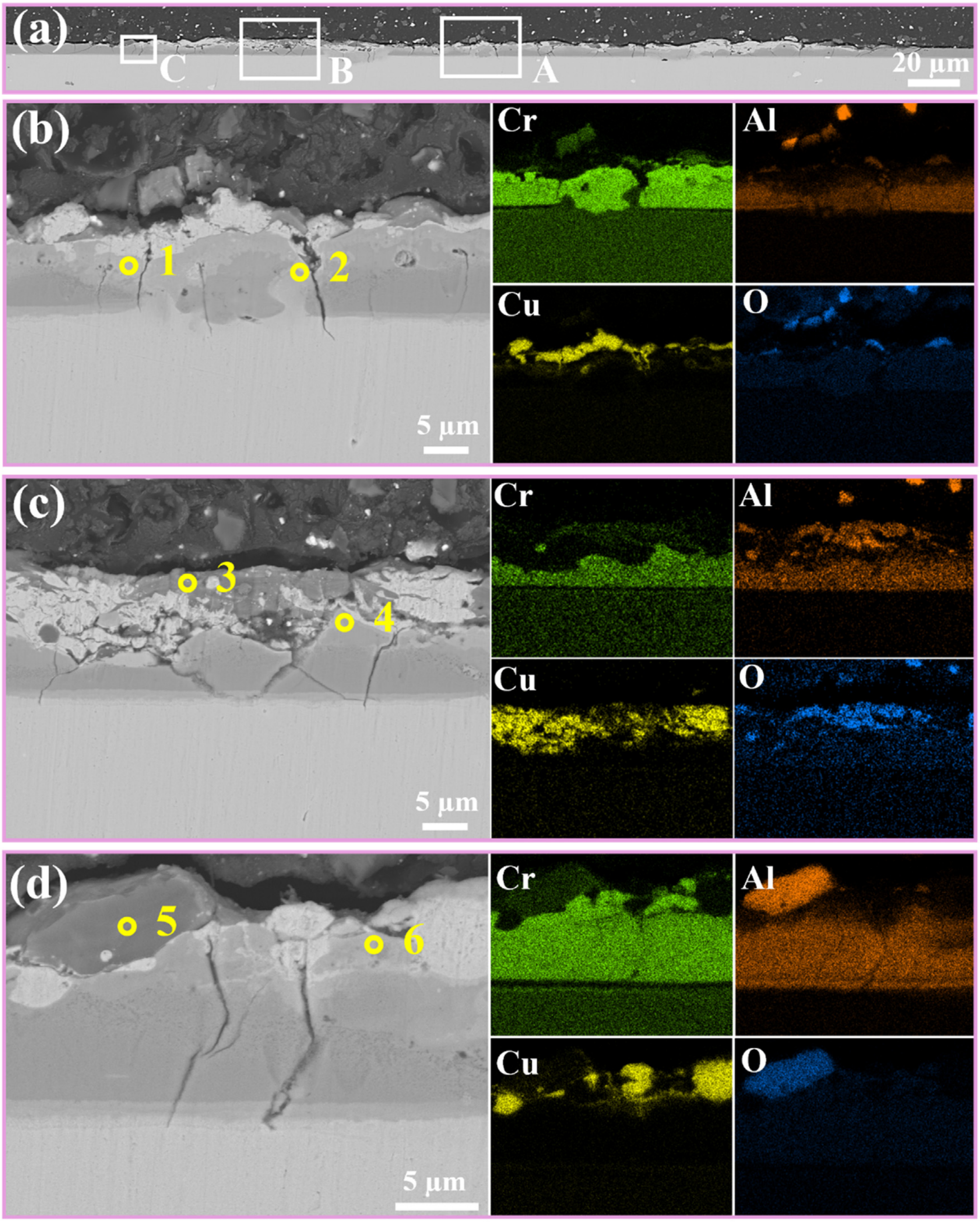

Fig. 7. (a) Arc erosion cross-sectional morphology of Cr_2AlC coating. (b) Central erosion area (Area A). (c) Transitional erosion area (Area B). (d) Edge erosion area (Area C).

where decomposed Al was captured and redistributed by the flowing melt before oxidizing at the surface.

The erosion boundary (Fig. 8(d)) shows the interface between the Cu-enriched melt and the unaffected coating. A comparison between Area 5 and Area 6 reveals an abrupt compositional discontinuity, with Area 6 showing a simultaneous increase in Ag and Al content. This suggests a synergistic migration mechanism driven by arc heat, where Ag and Al migrated from the Cr_2AlC structure toward the erosion front. Ag functioned as a transport medium by forming a low-melting-point alloy liquid with decomposed Al. This liquid phase subsequently flowed and solidified at the boundary, resulting in the observed surface accumulation.

3.5.2. Arc erosion cross-sectional morphology of Ag-Cr_2AlC coating

Fig. 9(a) shows the Ag-Cr_2AlC cross-sectional erosion morphology. Instead of the brittle fractures seen in pure Cr_2AlC coatings, Ag doping promotes the adhesion of large Cu blocks and eliminates macroscopic cracks. This shifts the failure mode from catastrophic brittle fracture to controlled, progressive ablation.

Fig. 9(b) reveals a robust bond between the Cu melt and the substrate. The corresponding element compositions are listed in Table 4. The presence of Ag in the Cu matrix (Area 1) confirms the formation of a Cu-Ag liquid alloy that enhances wetting. This creates a vertical conductive bridge, ensuring low contact resistance.

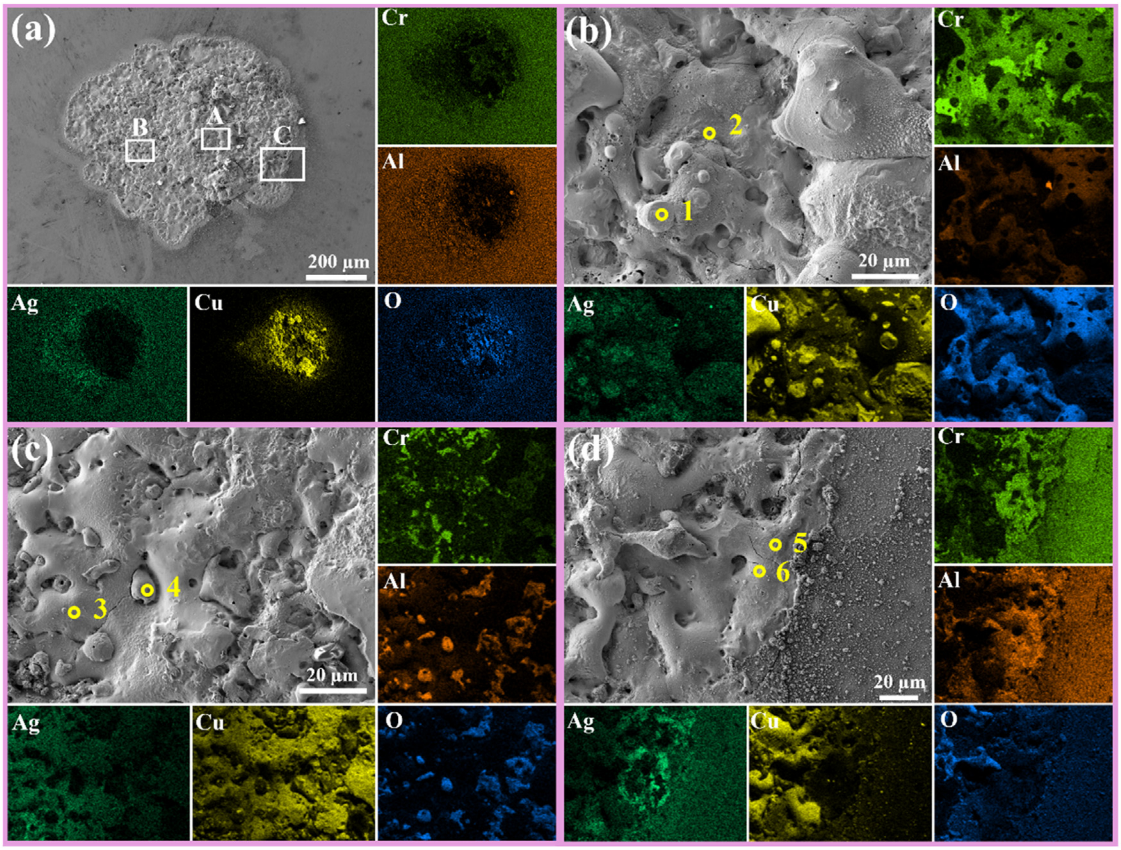

Fig. 8. (a) Arc erosion surface morphology of Ag-Cr_2AlC coating. (b) Central erosion area (Area A). (c) Transitional erosion area (Area B). (d) Edge erosion area (Area C).

Table 4
Elemental compositions of the corresponding regions (Area (at.%)) in Fig. 9.

	Area 1	Area 2	Area 3	Area 4	Area 5	Area 6	Area 7
C	39.96	41.62	13.43	34.73	37.91	24.57	29.42
O	5.29	3.94	47.60	2.75	4.05	1.67	2.16
Al	0.22	5.39	13.21	12.41	12.02	12.68	24.60
Cr	4.24	46.71	22.73	48.30	5.89	57.72	37.32
Cu	49.06	1.42	3.01	1.07	36.79	1.72	0.00
Ag	1.23	0.91	0.03	0.75	3.34	1.65	6.49

Meanwhile, Area 3 is dominated by Cr oxides, reflecting preferential Al depletion at the surface.

The transition erosion area (Fig. 9(c)) demonstrates that the anodic Cu melt has both covered the surface and infiltrated the coating. Analysis of the residual layer (Area 4) reveals significant depletion of Al and Ag, suggesting that these intrinsic elements reacted with the infiltrating melt to form a multicomponent alloy liquid. This intermixing is confirmed by the high Al and Cu concentrations found in the solidified melt at Area 5.

Fig. 9(d) shows the erosion boundary and thermo-ablative progression. Ag-enriched Cu splatters confirm a miscible Cu-Ag melt on the surface. Cr enrichment and Al depletion reflect the outward migration of an Al-Ag-Cu liquid phase (Area 6). This results in a stratified structure where Cr dominates the intermediate layer, while Al and Ag accumulate in the deeper substrate (Area 7).

4. Discussion

4.1. Thermodynamic driving forces and kinetic limitations

Based on existing literature reports and high-temperature oxidation experiments, the degradation behavior of Cr_2AlC in high-temperature environments has been systematically confirmed [25,37,38]. This provides a foundational baseline for elucidating the reaction mechanisms governing the instantaneous, ultra-high-temperature regime of electric arc erosion. Thermodynamically, Al exhibits a significantly lower Gibbs free energy of oxidation compared to Cr, dictating its preferential oxidation to form stable Al_2O_3. Concurrently, the rupture of Cr-Al bonds within the nanolaminated structure precipitates the collapse of the Cr_2AlC lattice, accompanied by the formation of the thermodynamically favored carbide phase, Cr_7C_3. The oxidation trajectory at this stage is described as [37]:

$$28Cr_2AlC\ (s) + 23O_2\ (g) = 8Cr_7C_3\ (s) + 14Al_2O_3\ (s) + 4CO\ (g) \tag{2}$$

Under conditions of extreme thermal load and oxygen saturation, the thermodynamic driving force overcomes the substantial Cr–C bond energy. This triggers the oxidation of Cr and C, leading to the complete decomposition of the MAX phase into a mixed oxide scale predominantly composed of Cr_2O_3 and Al_2O_3. The terminal oxidation pathway proceeds as follows [37]:

$$4Cr_2AlC\ (s) + 13O_2\ (g) = 4Cr_2O_3\ (s) + 2Al_2O_3\ (s) + 4CO_2\ (g) \tag{3}$$

However, the electric contact environment imposes unique kinetic constraints. During the current interruption, the arc root induces a transient temperature surge exceeding 3000 °C, followed by rapid quenching upon arc extinction. This extreme thermal shock induces the selective volatilization of Al and thermal decomposition of the matrix. Crucially, the non-equilibrium thermal cycling arrests diffusion-controlled kinetic processes, preventing thermodynamically anticipated reactions from reaching equilibrium.

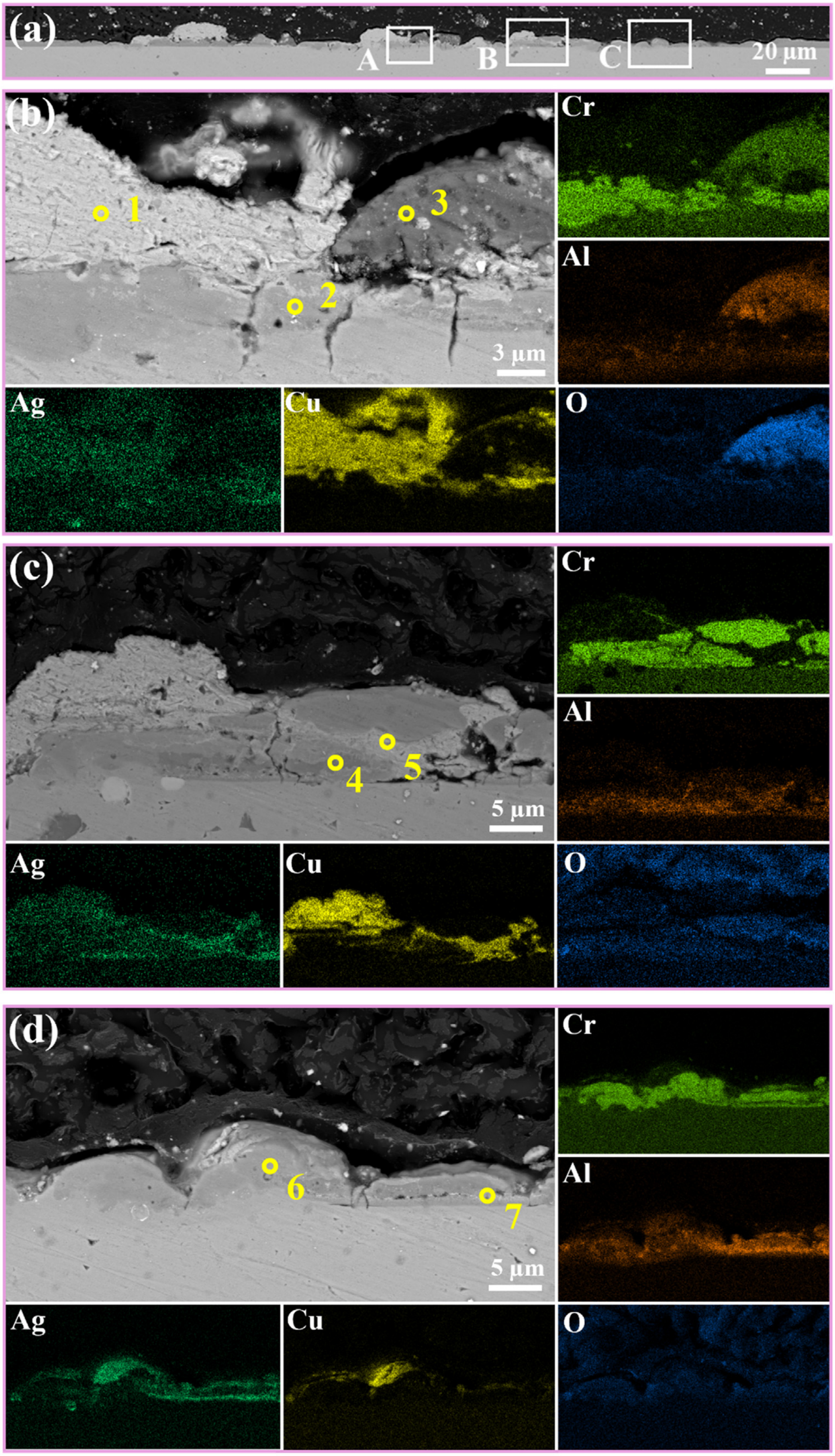

Fig. 9. (a) Arc erosion cross-sectional morphology of Ag-Cr_2AlC coating. (b) Central erosion area (Area A). (c) Transitional erosion area (Area B). (d) Edge erosion area (Area C).

This is exemplified in the central erosion zone, where a single, dense oxide scale fails to form; instead, an incomplete oxidation state characterized by multiphase coexistence persists.

4.2. Failure mechanism of pure Cr_2AlC: catastrophic brittle fracture

The post-mortem analysis of the Cr_2AlC cathode corroborates this high-temperature degradation mechanism. The cathode surface reveals substantial mass transfer of Cu from the anode, forming a distinct bulk melt in the central zone. The detection of Cr_7C_3 beneath this Cu layer validates the mechanism of preferential Al volatilization and structural decomposition. This severe ablation results in a complex stratification: a loosely adhered, Al-rich surface oxide, an intermediate Cu bonding layer, a Cr_7C_3 transition zone, and the pristine substrate. This multi-layered heterogeneous architecture is intrinsically vulnerable. Driven by the mismatch in CTE and the solidification shrinkage stress of Cu, cracks initiate at the Cu/oxide interface and propagate through the coating to the substrate. In the erosion transition zone, the non-uniform distribution of molten products further exacerbates localized thermal stress concentrations. Consequently, the pure Cr_2AlC coating exhibits three defining failure characteristics: anodic Cu transfer, multiphase decomposition, and stress-induced structural cracking. The schematic mechanism is depicted in Fig. 10(a).

4.3. The feedback loop of electrical degradation

Structural deterioration and oxide accumulation institute a deleterious positive feedback loop involving arcing duration and contact resistance. The prolongation of arcing time subjects the contact to higher thermal loads, promoting the accretion of insulating phases (Al_2O_3, Cr_2O_3) and carbides (Cr_7C_3). These high-resistance layers, combined with the arc-induced reduction in effective contact area, drive a sharp increase in contact resistance. Conversely, elevated contact resistance intensifies Joule heating, which in turn accelerates surface oxidation and volatilization, facilitating arc reignition or sustenance. This regenerative cycle ultimately manifests as a progressive degradation of switching performance.

4.4. Ag-mediated mechanism: benign sacrificial consumption

The divergence in failure modes between pure Cr_2AlC and Ag-Cr_2AlC is fundamental. While the pure coating suffers from brittle structural failure due to its equiaxed grain structure and lack of stress-relief avenues, the Ag-doped coating adopts a benign consumption mode. This is underpinned by two microstructural advantages: the small lath-like grain morphology and the strategic distribution of Ag at grain boundaries. In the Ag-Cr_2AlC system,

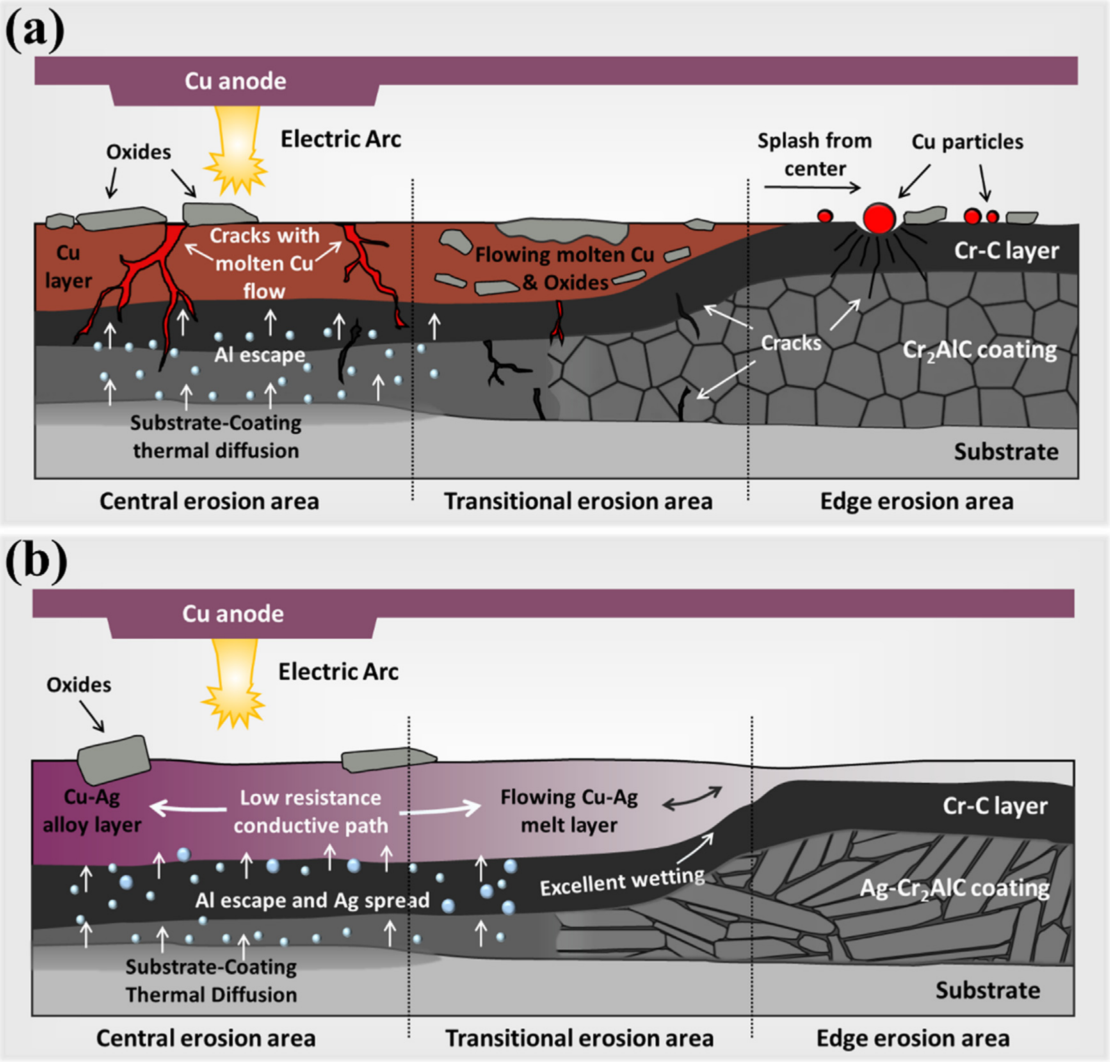

Fig. 10. (a) Cr_2AlC coating arc erosion mechanism. (b) Ag-Cr_2AlC coating arc erosion mechanism.

the intense arc heat rapidly activates the grain-boundary Ag. Leveraging the abundant channels provided by the lath-like structure, Ag migrates to the surface and reacts with anodic Cu to form a Cu-Ag liquid alloy. This alloy phase is critical: it significantly enhances the wettability of the melt on the ceramic decomposition products. This promotes the coalescence of the melt into stable droplets, thereby shielding the underlying structure from erosive penetration.

Distinctively, the ablation products of Ag-Cr_2AlC exhibit superior fluidity. In the erosion transition zone, the Cu-Ag melt spreads radially, driven by surface tension and thermal gradients. Because intrinsic Ag diffuses faster through grain boundaries than external Cu can infiltrate, a radial compositional gradient (decreasing Cu, increasing Ag) is established. Here, Ag acts as a flux, capturing decomposed Al and redistributing it to the surface, where it oxidizes to form Al_2O_3 precipitates.

Mechanically, this melt infiltrates the coating transversely (laterally) rather than vertically. This flexible infiltration effectively redistributes arc energy and alleviates thermal stress, in stark contrast to the vertical, penetrating cracks observed in pure Cr_2AlC. The failure mode thus transforms from stress-concentration-induced cracking to uniform thermo-ablative consumption (Fig. 10(b)).

4.5. Implications for electrical contact performance

This Ag-regulated mechanism is the microstructural basis for superior electrical performance. The metallic cladding layer formed by the conductive Cu-Ag alloy acts as a self-healing mechanism. It serves a dual function: (1) Displacing insulating oxides via fluid flow to maintain a clean contact interface; and (2) Establishing a low-resistance vertical percolation path (alloy bridges) through the coating. By maintaining a stable, low contact resistance, the Ag-Cr_2AlC coating effectively suppresses Joule heating, breaks the aforementioned feedback loop, and fundamentally shortens arcing time. Unlike the irreversible structural collapse of Cr_2AlC, the Ag-doped system operates via controlled sacrificial consumption. Late-stage performance fluctuations result from the gradual depletion of surface Ag rather than from catastrophic structural failure. The system sacrifices a portion of its thickness (consumption) to preserve structural integrity and electrical stability, representing a paradigm shift in contact material design.

5. Conclusions

Ag doping (~3.69 at.%) reprograms the Cr_2AlC coating into a lath-like architecture with a continuous Ag-rich grain-boundary network, enabling conductive percolation and activating a distinct arc-erosion pathway. In 24 V/3 A DC make-break tests for 1500 cycles, undoped Cr_2AlC exhibits unstable contact resistance, a welding/rupture event, and accelerated degradation after ~900 cycles with sharply increased arcing time and energy, whereas Ag-Cr_2AlC sustains low, stable arcing behavior and delays degradation to a much later stage with only micro-damage. Microstructural and compositional analyses show that arc-driven Cu transfer coupled with Ag redistribution produces a fluid Cu-Ag alloy/cladding layer that spreads laterally, replaces resistive oxides, forms low-resistance alloy bridges, and mitigates thermal-mismatch cracking, thereby converting catastrophic brittle failure into benign consumptive degradation. Together, these findings validate a coating design strategy utilizing grain-boundary metal networks to enable in situ conductive cladding, which breaks the synergistic feedback among resistance rise, Joule heating, and arcing, ultimately prolonging the service life of DC contacts.

Declaration of competing interest

The authors declare that they have no known competing financial interests or personal relationships that could have appeared to influence the work reported in this paper.

CRediT authorship contribution statement

Yingjie Wang: Writing – original draft, Methodology, Data curation. **Yuxi Xu:** Investigation, Data curation. **Yiqun Feng:** Methodology, Investigation. **Kaiwei Yang:** Methodology. **Qiang Wu:** Data curation. **Guanshui Ma:** Supervision. **Zhenyu Wang:** Writing – review & editing, Investigation, Funding acquisition. **Aiying Wang:** Writing – review & editing, Supervision, Funding acquisition, Conceptualization.

Acknowledgments

The work was financially supported by the National Key R&D Program of China (No. 2024YFB3816500), the Natural Science Foundation of Zhejiang Province (No. LR26E010004), and the Key Research and Development Program of Ningbo (Nos. 2024Z154 and 2024Z096).

References

[1] K. von Klinski-Wetzel, C. Kowanda, M. Heilmaier, F.E.H. Mueller, J. Alloy. Compd. 631 (2015) 237–247.
[2] V. Cosovic, A. Cosovic, N. Talijan, D. Zivkovic, D. Manasijevic, D. Minic, J. Alloy. Compd. 567 (2013) 33–39.
[3] M.T. Kesim, H. Yu, Y. Sun, M. Aindow, S.P. Alpay, Corros. Sci. 135 (2018) 12–34.
[4] X. Yuan, F. Fu, R. He, J. Mater. Sci. 59 (2024) 3762–3779.
[5] G. Li, X. Fang, W. Feng, J. Liu, J. Alloy. Compd. 716 (2017) 106–111.
[6] J. Xu, L. Zhou, G. Ma, G. Li, H. Zhao, H. Wang, J. Mater. Res. Technol. 31 (2024) 606–617.
[7] J. Yuan, Z. Wang, G. Ma, G. Zhou, X. Cheng, A. Wang, Acta Metall. Sin. 59 (2022) 961–968.
[8] B. Stelzer, X. Chen, P. Bliem, M. Hans, B. Völker, R. Sahu, C. Scheu, D. Primetzhofer, J.M. Schneider, Sci. Rep. 9 (2019) 8266.
[9] X. Huang, Y. Feng, G. Qian, Z. Zhou, Ceram. Int. 45 (2019) 20297–20306.
[10] T.A. Prikhna, O.P. Ostash, A.S. Kuprin, V.Y. Podhurska, T.B. Serbenyuk, E.S. Gevorkyan, M. Rucki, W. Zurowski, W. Kucharczyk, V.B. Sverdun, M.V. Karpets, S.S. Ponomaryov, B.D. Vasyliv, V.E. Moshchil, M.A. Bortnitskaya, Compos. Struct. 277 (2021) 114649.
[11] G. Ma, A. Zhang, Z. Wang, K. Wang, J. Zhang, K. Xu, Y. Xu, S. Zhou, A. Wang, Mater. Horiz. 12 (2025) 1689–1710.
[12] G. Wang, J. Zhou, W. Chen, J. Yang, J. Zhang, Y. He, Materials 14 (2021) 7068.
[13] F. Lin, Y. Xia, X. Feng, Friction 9 (2021) 774–788.
[14] J. Wang, C. Wang, Y. Kang, J. Alloy. Compd. 714 (2017) 698–703.
[15] X. Gui, L. Sun, C. Chen, Y. Yang, W. Gao, G. Gyawali, X. Liu, J. Ding, S. Zhang, Tribol. Int. 214 (2026) 111377.
[16] L. Sun, C. Chen, J. Hu, X. Liu, G. Gyawali, Y. Yang, K. Yang, X. Liu, S. Zhang, Tribol. Int. 214 (2026) 111245.
[17] D. Wang, H. Zhu, M. Zheng, Q. Tang, J. Xu, W. Wei, C. Lu, Z. Sun, J. Alloy. Compd. 961 (2023) 170870.
[18] J. Ding, W. Tian, D. Wang, P. Zhang, J. Chen, Y. Zhang, Z. Sun, Corros. Sci. 156 (2019) 147–160.
[19] X. Wu, C. Wu, X. Wei, W. Sun, C. Ma, Y. Zhang, G. Li, L. Chen, D. Wang, P. Zhang, Z. Sun, J. Ding, J. Adv. Ceram. 13 (2024) 176–188.
[20] J. Ding, W. Tian, D. Wang, P. Zhang, J. Chen, Y. Zhang, Z. Sun, J. Alloy. Compd. 785 (2019) 1086–1096.
[21] G. Zhang, Y. Shi, X. He, X. Chen, A. Duffy, M. Zhu, Z. Han, L. Wang, IEEE Trans. Compon. Packag. Manuf. Technol. 15 (2025) 140–149.
[22] W. Huang, H. Yu, L. Wang, X. Wu, C. Ouyang, Y. Zhang, J. He, Mater. Today Commun. 37 (2023) 107256.
[23] Z. Wang, J. Liu, L. Wang, X. Li, P. Ke, A. Wang, Appl. Surf. Sci. 396 (2017) 1435–1442.
[24] X. Chen, B. Stelzer, M. Hans, R. Iskandar, J. Mayer, J.M. Schneider, Mater. Res. Lett. 9 (2021) 127–133.
[25] Z. Wang, G. Ma, L. Liu, L. Wang, P. Ke, Q. Xue, A. Wang, Corros. Sci. 167 (2020) 108492.
[26] G. Ma, H. Wu, Z. Fang, X. Zhou, R. Chen, W. Yang, J. Zhang, Z. Wang, A. Wang, J. Mater. Sci. Technol. 206 (2025) 176–184.
[27] C.A. Huerta-Aguilar, Y.S. García Gutiérrez, P. Thangarasu, Chem. Eng. J. 394 (2020) 124286.
[28] Y. Dong, Z. Wang, J. Yuan, Z. Wang, Y. Zhang, G. Ma, A. Wang, Wear 540–541 (2024) 205221.
[29] W. Ren, C. Zhang, X. Sun, IEEE Access 8 (2020) 93857–93867.
[30] Y. Champion, Y. Bréchet, Adv. Eng. Mater. 12 (2010) 798–802.

[31] K. Liang, F. Wang, L. Zhong, S. Chen, Q. Sun, X. Duan, S. Liu, IEEE Trans. Dielectr. Electr. Insul. 31 (2024) 747–755.
[32] X. Wang, S. Wei, C. Zhang, L. Xu, H. Yu, L. Yang, K. Pan, H. Wang, X. Cao, J. Mater. Sci. 59 (2024) 1635–1651.
[33] J. Zhang, M. Zhou, J. Xu, Y. Zhang, K. Jing, C. Chu, L. Li, B. Tian, X. Li, H. Guo, J. Alloy. Compd. 1022 (2025) 179824.
[34] P. Hu, B.L. Hu, K.S. Wang, F. Yang, R. Song, Z.T. Yu, Q. Wang, W.C. Cao, D.X. Liu, G. An, L. Guo, H. Yu, J. Alloy. Compd. 685 (2016) 465–470.
[35] H. Tang, X. Yin, P. Zhang, V. Karpov, V. Borra, Z. Tian, W. Zheng, J. Ding, Z. Sun, Ceram. Int. 50 (2024) 43013–43022.
[36] X. Fan, X. Ma, X. Dang, J. Xue, F. Ye, D. Zhao, L. Cheng, J. Eur. Ceram. Soc. 40 (2020) 3414–3422.
[37] Z.J. Lin, M.S. Li, J.Y. Wang, Y.C. Zhou, Acta Mater. 55 (2007) 6182–6191.
[38] J.L. Smialek, J.A. Nesbitt, T.P. Gabb, A. Garg, R.A. Miller, Mater. Sci. Eng. A 711 (2018) 119–129.